Journal of
Materials Chemistry C

Materials for optical, magnetic and electronic devices

rsc.li/materials-c

ROYAL SOCIETY
OF CHEMISTRY
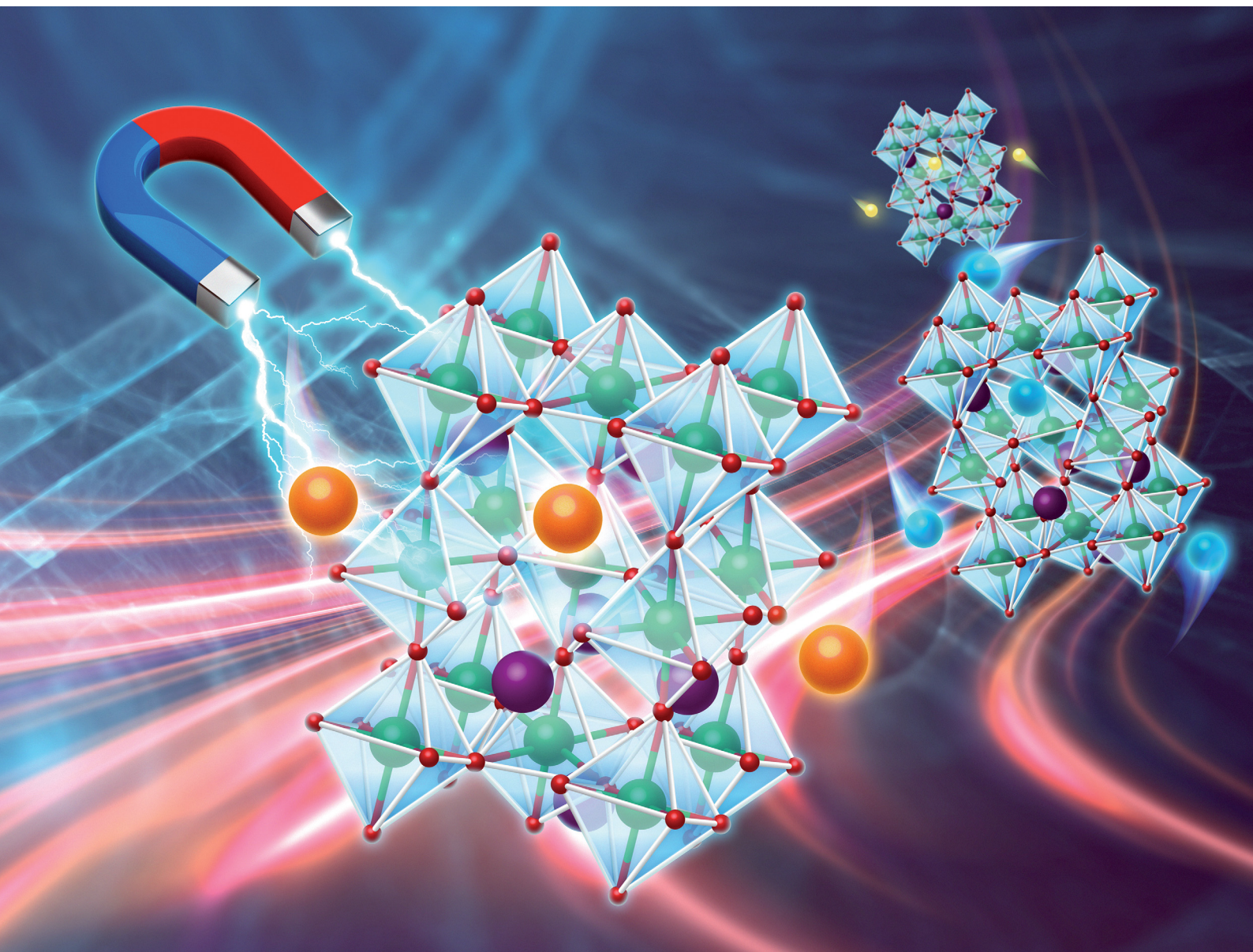
PAPER
Katsuhisa Tanaka *et al.*
Crystal structure and magnetic properties of EuZrO₃ solid
solutions

10 YEARS ANNIVERSARY

ROYAL SOCIETY
OF CHEMISTRY

Check for updates

Crystal structure and magnetic properties of EuZrO₃ solid solutions†

Sihui Li, [ID] * Shinya Konishi, [ID] Takuya Kito, Koji Fujita [ID] and Katsuhisa Tanaka [ID] *

It is theoretically proposed that perovskite-type $EuZrO_3$ becomes a ferromagnet when the lattice volume is increased or the structure is changed from orthorhombic to cubic in contrast to the fact that the stable phase of $EuZrO_3$, the structure of which is orthorhombic, is antiferromagnetic. To investigate the change in crystal structure and magnetic properties of $EuZrO_3$ with the variation of lattice volume, we have synthesized polycrystals of solid solutions $A_xEu_{1-x}ZrO_3$ (A = Ba, Ca, Sr); Eu^{2+} is substituted by group 2 elements with different ionic radius to realize the change in lattice volume and crystal structure of $EuZrO_3$. The stable magnetic structure of $EuZrO_3$ solid solutions is tuned with the change of lattice volume. In particular, the ferromagnetic state is stabilized by the increase in lattice volume, which experimentally verifies the prediction by the first-principles calculations. Furthermore, this phenomenon is explainable in terms of the competition between ferromagnetic and antiferromagnetic interactions that is highly related to the volume variation and the rotation of ZrO_6 octahedron. The present results indicate that the magnetic structure can be systematically tuned by controlling the chemical pressure in solid solutions.

1. Introduction

Multiferroics display two or more primary ferroic orderings, such as ferroelectricity (FE), ferro-, antiferro-, or ferri-magnetism, ferrotoroidicity, and ferroelasticity in a single-phase, and the coupling between these multiple order parameters leads to novel effects, specifically, the magnetoelectric (ME) effect.[1–3] Much attention has been paid to the multiferroic properties of perovskite-type oxides the composition of which is denoted by ABO_3, especially since the discovery of enhancement of polarization in constrained thin films of ferroelectromagnet $BiFeO_3$ and manipulation of the electric polarity of $TbMnO_3$ with a magnetic field.[4,5] Currently, studies of ABO_3 perovskite oxides with ME effect have focused on several compounds including divalent europium-based perovskite oxides with a general formula of $EuMO_3$ (M: group 4 elements).[6] For the multiferroic $EuMO_3$, the correlation between magnetic and dielectric properties through the spin-lattice coupling was experimentally demonstrated for $EuTiO_3$ (paraelectric and G-type antiferromagnetic).[7–9] Specifically, the dielectric constant manifests a drastic drop at the antiferromagnetic phase transition temperature, *i.e.*, the Néel temperature (T_N), due to the hardening of soft phonon modes and subsequent saturation disruption of the dielectric constant

at low temperature. The decrease of dielectric constant can be suppressed by applying a magnetic field below T_N and the dielectric constant is altered by 7% at 1.5 T, corresponding to a large ME effect.[9] Moreover, ferromagnetism of $EuTiO_3$ (ETO) induced by an external electric field exhibits another aspect of ME effect.[10] Such an ME effect was observed for $EuZrO_3$ as well.[11] For magnetic properties closely related to the ME effect of $EuMO_3$, the critical balance was proposed between the antiferromagnetic (AFM) superexchange interaction *via* the nd orbitals of M elements and ferromagnetic (FM) indirect exchange interaction *via* the Eu 5d states based on the hybrid Hartree–Fock density functional calculations.[12]

Due to the strong correlation between the degrees of freedom in crystal structure and order parameters related to the dielectric and magnetic properties, ME effects can be modified *via* various engineering techniques.[13–22] Density functional theory (DFT) calculations and subsequent experiments have proposed that through the strain engineering, ETO thin film deposited on a substrate can be converted from a paraelectric (PE)-AFM phase to a FE-FM phase.[23,24] A change in the magnetic interactions of FM ordering induced by engineering techniques in $EuMO_3$ is anticipated to modify the ME effects. The influence of engineering techniques including strain and stress as well as lattice volume change on the magnetic structure and properties of ETO has been studied theoretically and experimentally. DFT calculations revealed that when a biaxial compressive strain is induced in the surface, both FM and FE states become stable in ETO thin films.[23] This was supported by

Department of Material Chemistry, Graduate School of Engineering, Kyoto University, Nishikyo-ku, Kyoto 615-8510, Japan. E-mail: li.sihui.26k@st.kyoto-u.ac.jp, tanaka.katsuhisa.4n@kyoto-u.ac.jp

This journal is © The Royal Society of Chemistry 2023

J. Mater. Chem. C, 2023, 11, 8383–8392 | 8383

the appearance of nanometer-sized FM clusters in ETO films when an electric field is applied under a moderate compressive strain.[10] The observation of FM properties has been also reported for ETO thin films with a in-plane biaxial tensile strain and a vertical strain.[25–27] Furthermore, it was suggested by the hybrid Hartree–Fock density functional calculations that the lattice volume-expanded $EuMO_3$ prefers the FM interaction through the Eu 5d states to the AFM one *via* the M nd states, as a consequence of the reduced hybridization of the Eu 4f and M nd orbitals.[28] The volume expansions induced by the lattice mismatch between ETO thin films and different substrates can change the magnetic ground state of ETO from AFM to FM, experimentally supporting the theoretical calculations.[29] Based on the critical balance between AFM superexchange interaction *via* the M nd orbitals and FM indirect exchange interaction *via* Eu 5d states, the FM state resulting from the modification of crystal structure of $EuMO_3$ by engineering techniques was confirmed by the works mentioned above. However, those works were conducted on biaxially strained $EuMO_3$ thin films, and the strain engineering was restricted by the substrate and could not realize three-dimensionally isotropic volume change. On the other hand, a uniform three-dimensional strain-induced negative pressure was realized by Zhao *et al.*[30] in a composite thin film of $EuTiO_3$ in which MgO phases of cylindrical shape were embedded. They observed the FM state in the ETO nanocomposite film and explained the magnetic state in terms of a different critical balance between the out-of-plane AFM nearest exchange interaction and the in-plane FM exchange interaction. Thus, the mechanism of the magnetic interaction in $EuMO_3$ under three-dimensional strain or stress remains controversial.

$EuZrO_3$, another kind of $EuMO_3$, shows an orthorhombic crystal structure (*Pbnm*) and exhibits structural distortions associated with octahedral rotations, thereby having a lower symmetry than the ETO which adopts the ideal cubic ($Pm\bar{3}m$) perovskite structure.[31–34] As for the magnetism, Eu^{2+} ions in $EuZrO_3$ favor the G-type AFM structure, which has been verified by the analysis of the sign and magnitude of the magnetic exchange constants based on the Heisenberg spin Hamiltonian.[6,35] This theoretical analysis along with experimental observations of the AFM transition at 4.1 K indicates that $EuZrO_3$ is magnetically similar to ETO.[11,34] Moreover, the calculations by Akamatsu *et al.* propose that the exchange coupling constant also can be varied by the lattice volume, showing its potential for modulating the magnetic order.[28] This prediction provided an insight that not only the volume expansion of lattice but the decrease of octahedral rotation involved in the structural change from orthorhombic *Pbnm* to cubic $Pm\bar{3}m$ structures leads to the weakening of the AFM interaction *via* Zr 4d orbitals and even triggering the occurrence of FM order in $EuZrO_3$. Furthermore, the calculations extended an understanding of the competition between AFM superexchange interaction *via* the M nd orbitals and FM indirect exchange interaction *via* Eu 5d states in $EuMO_3$.

A chemical pressure, often observed in solid solutions, can induce the three-dimensional strain or stress, which is important to clarify the mechanism of magnetic interaction in $EuMO_3$ as mentioned above, and can change the lattice volume

as well as crystal structure that has influence on the magnetic interactions and structures.[29,36,37] The formation of solid solutions through the A-site cation substitution has been reported to modulate the lattice volume and the accompanying structural evolution of ABO_3 perovskite oxides.[38–43] The alkaline earth metal zirconates $AZrO_3$ (A = Ba, Ca and Sr) have different crystal structures and crystal lattice volumes at room temperature; the structure is cubic $Pm\bar{3}m$ for A = Ba and orthorhombic *Pbnm* for A = Ca and Sr.[44–48] Thus, the substitution of the A-site (Eu^{2+}) by group 2 elements has the potential to induce variations in lattice volume and crystal structure and to fine-tune the magnetic properties of $EuZrO_3$. In this study, we aimed to qualitatively verify the theoretical prediction deduced by Akamatsu *et al.* and reveal the underlying intrinsic mechanism of tuning the relative strengths of the competing magnetic interactions by changing the lattice volume for $EuZrO_3$.[28] The change of magnetic ordering state of $EuZrO_3$ with a systematic variation in the lattice volume was experimentally elucidated by an A-site substitution. Through a conventional solid-state reaction method, the A-site (Eu^{2+}) substitution was realized by group 2 elements (Ba, Ca, and Sr) with different ionic radii. The lattice volume, crystal structure, local environment, chemical state of europium ions, and magnetic properties of solid solutions $A_xEu_{1-x}ZrO_3$ (A = Ba, Ca, and Sr) were investigated using powder X-ray diffraction (XRD), high-resolution X-ray fluorescence spectrometry (HRXRF), and superconducting quantum interference device (SQUID) magnetometer. We found that the solid solutions based on $EuZrO_3$ are AFM even when Sr^{2+} or Ca^{2+} is incorporated and an enhanced AFM behavior is observed in $Ca_{0.3}Eu_{0.7}ZrO_3$ while the ferromagnetic ordering occurs in $Ba_{0.3}Eu_{0.7}ZrO_3$. Overall, this study demonstrates the correlation between magnetic structure at low temperatures and the lattice volume of the $EuZrO_3$ solid solutions. It is an important point that under the scenarios of three-dimensional chemical pressure, the present study provides direct evidence to control the competition between AFM and FM interactions among Eu^{2+} ions by changing the ZrO_6 octahedral rotation.

2. Results and discussion

2.1. Structural characterization

The structural characterization was performed at room temperature in the present study. It is known that $EuZrO_3$ takes the orthorhombic *Pbnm* structure with the lattice parameters at room temperature (a = 5.8192 Å, b = 8.1958 Å, and c = 5.7958 Å) and 1.4 K (a = 5.8163 Å, b = 8.1854 Å, and c = 5.7816 Å).[49] For $BaZrO_3$ with space group $Pm\bar{3}m$ and $SrZrO_3$ with space group *Pbnm*, the normalized molar volume approximately changes from 1.000 to 1.003 and 1.000 to 1.004, respectively, when the temperature is varied from 4.2 to 300 K.[50] In addition, $CaZrO_3$ with *Pbnm* structure has an average volume thermal expansion coefficient of 8.5192×10^{-6} K^{-1} at temperatures from approximately 0 to 350 K. Thus, the crystal structures of the $A_xEu_{1-x}ZrO_3$ series remains stable even if the temperature is varied from room temperature (300 K) to very low temperature.[51]

8384 | *J. Mater. Chem. C*, 2023, **11**, 8383–8392

This journal is © The Royal Society of Chemistry 2023

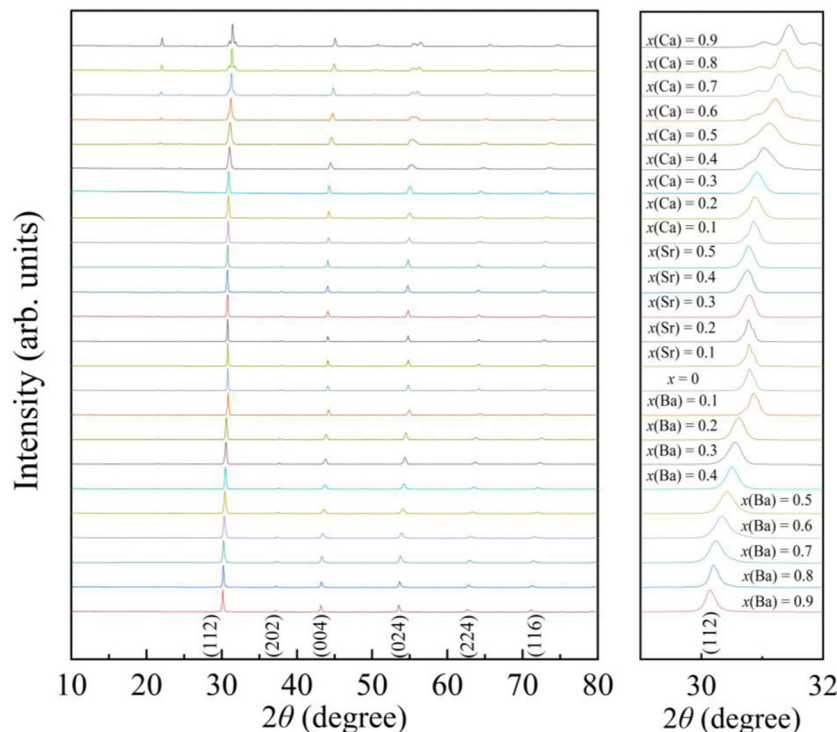**Fig. 1** The powder X-ray diffraction (XRD) patterns of $A_xEu_{1-x}ZrO_3$ ($0 \leq x \leq 1$), where A is Ca, Sr, or Ba. The right panel shows enlarged patterns of the most intense peak for samples.

The powder X-ray diffraction (XRD) patterns of the $A_xEu_{1-x}ZrO_3$ series recorded at $\sim$300 K are shown in Fig. 1. Each of the samples is almost entirely composed of a single phase with perovskite structure, although a trace amount of ZrO_2 is detectable as an impurity phase in most of the $A_xEu_{1-x}ZrO_3$ series (Fig. S1, ESI†). Compared to pure $EuZrO_3$, the diffraction peaks systematically shift to lower angles upon the incorporation of the larger Ba^{2+}. This result confirms an increase in the unit lattice volume of $Ba_xEu_{1-x}ZrO_3$ solid solutions, as the ionic radius of Ba^{2+} in coordination number (CN) 8 (1.61 Å) is larger than that of Eu^{2+} (1.43 Å) in CN 8.[48] In contrast, oposite diffraction peak shifts are observed when the Eu^{2+} is substituted by Ca^{2+} in CN 8 (1.37 Å), indicating a smooth lattice contraction for all synthesized members of $Ca_xEu_{1-x}ZrO_3$. Additionally, since the ionic radius of Sr^{2+} in CN 8 (1.44 Å) is almost the same as Eu^{2+}, no apparent peak shift is observed for $Sr_xEu_{1-x}ZrO_3$ as shown in Fig. 1.[48] All trends in XRD patterns indicate that the replacement of Eu^{2+} with group 2 elements is indeed an effective strategy for compositional tuning of lattice volume by utilizing the chemical pressure.

Part of the result of Rietveld analysis is illustrated in Fig. 2. All the patterns were well described by assuming that the sample was composed of a single-phase. Based on the refinement results, all the solid solutions are assigned to most probable space group. Fig. 2a confirms that $EuZrO_3$ is identified as an orthorhombic unit cell with space group $Pbnm$ and the lattice constants, which are in good agreement with the values reported previously.[33,34] Moreover, the XRD patterns of $Ca_xEu_{1-x}ZrO_3$ and $Sr_xEu_{1-x}ZrO_3$ solid solutions are assigned to

orthorhombic $Pbnm$ structure, coincident with the fact that $EuZrO_3$, $CaZrO_3$ and $SrZrO_3$ have the same structure.[44–46] For $Ba_xEu_{1-x}ZrO_3$ solid solutions, because $BaZrO_3$ takes a cubic structure with $Pm\bar{3}m$ space group at room temperature, the phase is changed from orthorhombic $Pbnm$ to cubic $Pm\bar{3}m$ with an increase in Ba concentration.[44,47,52] The $Pbnm$ and $Pm\bar{3}m$ structure are represented by $a^-a^-c^+$ and $a^0a^0a^0$ of Glazer notation, respectively.[32] The sequence of phases in the $Ba_xEu_{1-x}ZrO_3$ series at room temperature and the accompanying crystal symmetry can be deduced as follows (Table 1): $0 \leq x \leq 0.3$, orthorhombic $Pbnm$ ($a^-a^-c^+$); $0.4 \leq x \leq 0.6$, orthorhombic $Ibmm$ ($a^-a^-c^0$); $x = 0.7$, tetragonal $I4/mcm$ ($a^0a^0c^-$); and $0.80 \leq x \leq 1$, cubic $Pm\bar{3}m$ ($a^0a^0a^0$).[28] These deductions agree with the results given by Howard and Stokes for structural transition of ABO_3 perovskites. All of the fitted patterns are given in Fig. S1 (ESI†).[38,53]

Gradual changes in the lattice constants and volume induced by A-site isovalent substitution are found from the results of refinement (Table 1), and the correlation between the composition x and the lattice volume for the $A_xEu_{1-x}ZrO_3$ series is clearly seen in Fig. 3. All the compositional dependences of lattice volume follow the Vegard's law.[54,55] The lattice volume linearly increases, linearly decreases, and remains constant with Ba, Ca, and Sr concentrations, respectively, confirming the formation of all-proportional solid solutions.

2.2 Magnetic properties

The temperature dependence of magnetic susceptibility χ (T) was obtained *via* field-cooling (FC) process under an applied

This journal is © The Royal Society of Chemistry 2023

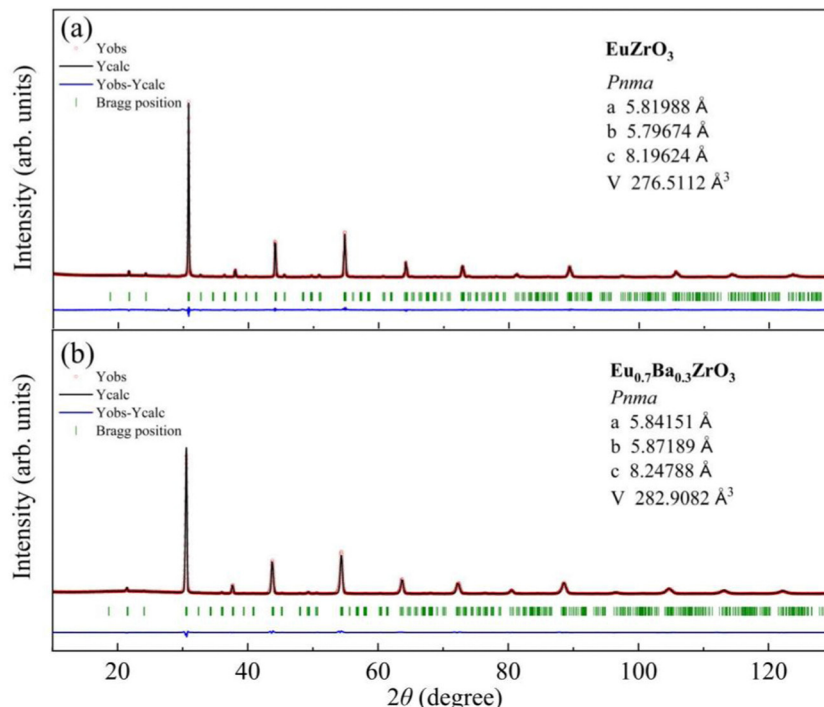*J. Mater. Chem. C*, 2023, **11**, 8383–8392 | **8385**

Fig. 2 X-ray diffraction profiles measured at room temperature (red crosses) and calculated profiles obtained by Rietveld analysis (black solid curves) for (a) $EuZrO_3$, and (b) $Ba_{0.3}Eu_{0.7}ZrO_3$. The vertical ticks (green) indicate the positions of the Bragg reflections, and the bottom solid lines (blue) correspond to the difference between the observed and the calculated intensity.

Table 1 Refined Structural Parameters for $A_xEu_{1-x}ZrO_3$ with A = Ba, Ca, and Sr ($0 \leq x \leq 0.9$)

$Ba_xEu_{1-x}ZrO_3$	a (Å)	b (Å)	c (Å)	V (Å^3)	Space group	R_{wp} (%)	R_B (%)	S
$x = 0$	5.79674(4)	5.81988(4)	8.19624(5)	276.511(3)	$Pbnm$	2.316	4.799	1.746
$x = 0.1$	5.82575(8)	5.81277(7)	8.20967(9)	278.010(5)	$Pbnm$	10.29	6.814	2.208
$x = 0.2$	5.83588(8)	5.84784(8)	8.23440(11)	281.017(6)	$Pbnm$	10.12	7.702	2.200
$x = 0.3$	5.84151(11)	5.87189(11)	8.24788(16)	282.908(9)	$Pbnm$	10.77	8.171	2.370
$x = 0.4$	5.86280(13)	5.85745(12)	8.27547(19)	284.188(10)	$Ibmm$	5.573	3.922	3.719
$x = 0.5$	5.88447(10)	5.87592(9)	8.28320(14)	286.405(8)	$Ibmm$	3.681	4.087	2.466
$x = 0.6$	5.90892(12)	5.89129(12)	8.31516(18)	289.460(10)	$Ibmm$	5.315	4.192	3.608
$x = 0.7$	5.90694(10)	5.90694(10)	8.32721(14)	290.552(8)	$I4/mcm$	7.046	5.115	4.647
$x = 0.8$	4.18186(3)			73.1322(9)	$Pm\bar{3}m$	6.544	4.316	3.956
$x = 0.9$	4.18862(2)			73.4873(7)	$Pm\bar{3}m$	6.110	5.148	3.695

$Ca_xEu_{1-x}ZrO_3$	a (Å)	b (Å)	c (Å)	V (Å^3)	Space group	R_{wp} (%)	R_B (%)	S
$x = 0.1$	5.77804(6)	5.81272(6)	8.17967(9)	274.723(5)	$Pbnm$	2.529	4.348	2.154
$x = 0.2$	5.75758(6)	5.80380(6)	8.16325(9)	272.781(5)	$Pbnm$	2.437	8.470	2.927
$x = 0.3$	5.75090(5)	5.79130(5)	8.16550(8)	271.953(4)	$Pbnm$	2.452	4.521	2.505
$x = 0.4$	5.72996(14)	5.80064(15)	8.15116(20)	270.923(11)	$Pbnm$	3.554	7.375	2.638
$x = 0.5$	5.71224(20)	5.79369(20)	8.13813(28)	269.331(16)	$Pbnm$	11.84	8.138	2.638
$x = 0.6$	5.69244(15)	5.78965(16)	8.11824(21)	267.554(12)	$Pbnm$	4.261	6.172	4.664
$x = 0.7$	5.65930(7)	5.77553(7)	8.07929(10)	264.075(6)	$Pbnm$	3.626	3.741	3.414
$x = 0.8$	5.64155(6)	5.77700(7)	8.07081(9)	263.037(5)	$Pbnm$	3.580	3.658	3.982
$x = 0.9$	5.61377(9)	5.75465(10)	8.03228(13)	259.485(7)	$Pbnm$	5.085	2.238	4.467

$Sr_xEu_{1-x}ZrO_3$	a (Å)	b (Å)	c (Å)	V (Å^3)	Space group	R_{wp} (%)	R_B (%)	S
$x = 0.1$	5.79485(2)	5.81957(2)	8.19647(3)	276.413(2)	$Pbnm$	2.817	5.870	0.246
$x = 0.2$	5.79604(2)	5.81993(2)	8.20028(4)	276.616(2)	$Pbnm$	2.748	3.294	0.216
$x = 0.3$	5.79672(19)	5.82203(20)	8.19981(28)	276.732(17)	$Pbnm$	8.621	7.278	2.205
$x = 0.4$	5.79668(2)	5.82164(2)	8.20036(4)	276.730(2)	$Pbnm$	2.131	3.408	2.252
$x = 0.5$	5.79763(4)	5.82151(4)	8.20247(6)	276.841(4)	$Pbnm$	10.32	6.961	2.278

magnetic field of 100 Oe for $A_xEu_{1-x}ZrO_3$. The results are illustrated in Fig. 4. The $\chi(T)$ curve for the zero-field-cooling (ZFC) process coincides with that for the FC process within experimental errors. The magnetic phase transition temperatures
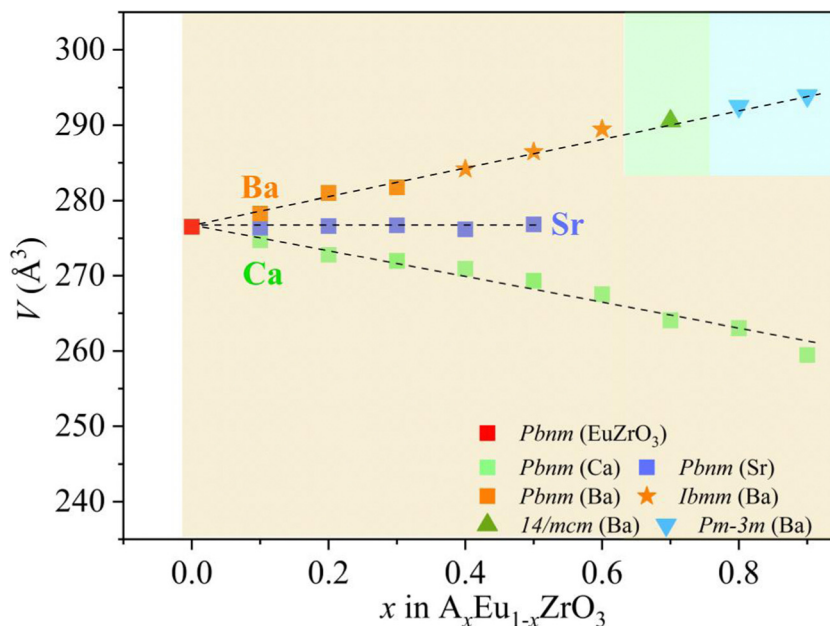
8386 | *J. Mater. Chem. C*, 2023, **11**, 8383–8392

This journal is © The Royal Society of Chemistry 2023

Fig. 3 Compositional dependence of the lattice volume of unit cell (V) at room temperature for the solid solutions $A_x Eu_{1-x} ZrO_3$. The difference in shape and color of the symbols correspond to the difference in the space groups and the alkaline earth metal elements, respectively. The background color represents the structure of the solid solutions; yellow for orthorhombic, pale green for tetragonal, and pale blue for cubic.

(Néel temperature, T_N and Curie temperature, T_C) were acquired by taking the 1st derivation of $\chi(T)$ curves. The results are summarized in Table 2. Since the presence of a trace trivalent europium (6%) is confirmed by ^{151}Eu Mössbauer spectroscopy and high-resolution X-ray fluorescence spectrometry (Fig. S2 and S3, ESI†), both Curie paramagnetism of Eu^{2+} and Van Vleck paramagnetism of Eu^{3+} are taken into consideration for analyzing the magnetic susceptibility of $A_x Eu_{1-x} ZrO_3$ solid solutions in the high-temperature region. In the present case, the following equations were used:

$$\chi = n\chi_{Eu^{2+}} + (1-n)\chi_{Eu^{3+}} + \chi_0 \qquad (1)$$

$$\chi_{Eu^{2+}} = \frac{N M_B^2 \mu_B^2}{3 k_B (T - \theta_w)} \qquad (2)$$

$$\chi_{Eu^{3+}} = \frac{N \mu_B^2}{3 k_B} \times \frac{24/a + (13.5 - 1.5/a)e^{-a} + (67.5 - 2.5/a)e^{-3a} + (189 - 3.5/a)e^{-6a}}{1 + 3e^{-a} + 5e^{-3a} + 7e^{-6a}} \qquad (3)$$

In eqn (1), n is the molar ratio of Eu^{2+} to the total europium ions the value of which is 0.94 (Fig. S2 and S3, ESI†), χ_0 is the temperature-independent term. $\chi_{Eu^{2+}}$ is the magnetic susceptibility of Eu^{2+} according to the Curie–Weiss law [eqn (2)], where N is the number of magnetic moment, k_B is the Boltzmann constant, μ_B is the Bohr magneton, and M_B is the effective number of Bohr magnetons with the theoretical value of 7.94. $\chi_{Eu^{3+}}$ is the magnetic susceptibility of trivalent Eu ions based on the Van Vleck paramagnetism [eqn (3)], where a ($a = \lambda/k_B T$) is the ratio of the multiplet width with the value of 370 cm^{-1} for the spin–orbit coupling constant λ.[56,57] The experimental data are fitted well with the theoretical curves (Fig. S4, ESI†).

The Weiss temperature (θ_W) obtained by the fitting was also listed in Table 2.

The present $EuZrO_3$ sample manifests a clear AFM transition (T_N = 4.1 K) in line with the previous study.[11,34] The $A_x Eu_{1-x} ZrO_3$ (A = Ca, Sr) solid solutions also exhibit AFM behavior for x = 0.1–0.4 while PM behavior is observed for x = 0.5 due to the dilution of magnetic moment assigned to Eu^{2+} ion. Besides, $Ba_x Eu_{1-x} ZrO_3$ solid solutions with x = 0.1 and 0.2 show AFM-like behavior. When x reaches 0.3, the compound exhibits FM behavior; the magnetization drastically increases below T_C with a decrease of temperature.[58] For x = 0.4 and 0.5, since significant magnetic dilution reduces the spin–spin interactions, magnetic ordering is not observed and the compounds show PM behavior.

The Weiss temperature, θ_W, reflects the magnitude and the sign of the magnetic interaction among Eu^{2+} ions. For $Ba_x Eu_{1-x} ZrO_3$, as the fraction of Ba is increased, θ_W initially increases from −0.19 (x = 0) to 0.67 (x = 0.3), and subsequently decreases to 0.15 (x = 0.5). The change of sign of θ_W from negative to positive when x increases from 0 to 0.3 suggests that the dominant interaction is switched from AFM to FM when the fraction of Ba is increased up to x = 0.3. The switch of magnetic interaction reflects the fact that the AFM and FM interactions compete with each other in $EuZrO_3$. The value of θ_W is decreased dramatically above x = 0.4 and the compounds are PM even at low temperatures as indicated by Fig. 4(a). For $Sr_x Eu_{1-x} ZrO_3$, due to the weakening of AFM interaction caused
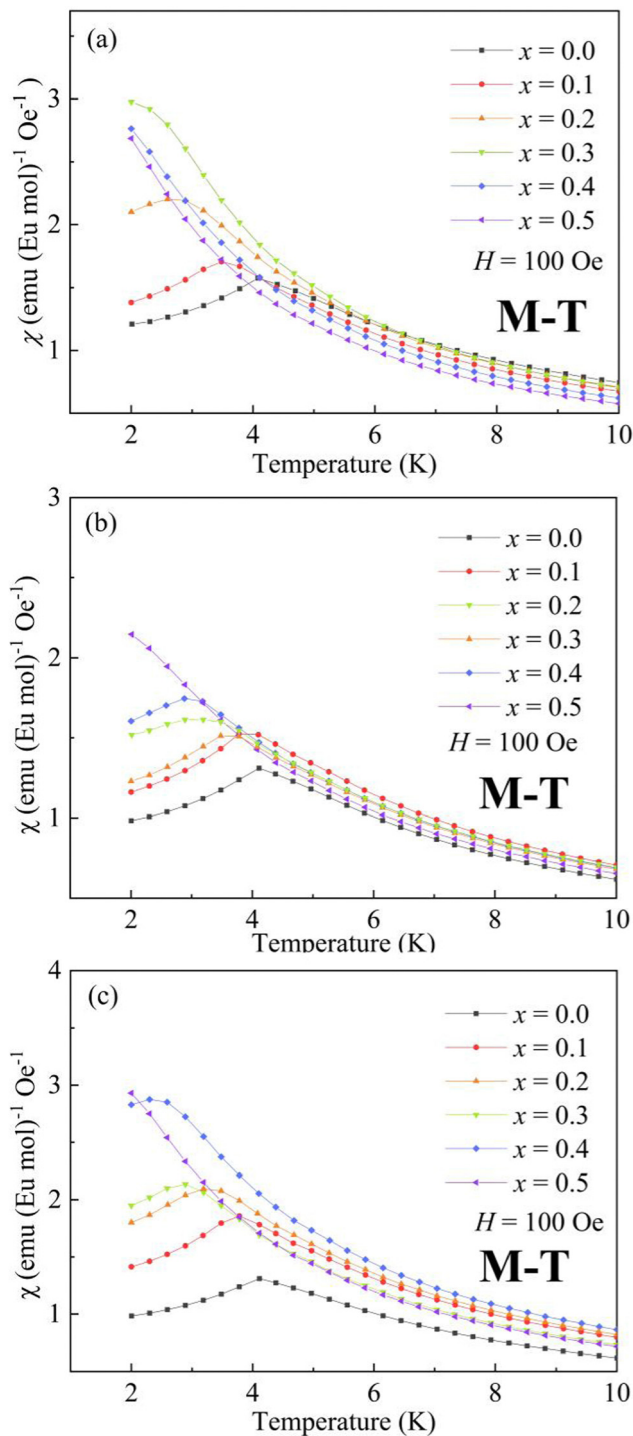
This journal is © The Royal Society of Chemistry 2023

J. Mater. Chem. C, 2023, **11**, 8383–8392 | **8387**

Fig. 4 Temperature dependence of magnetic susceptibility χ (T) for (a) $Ba_xEu_{1-x}ZrO_3$, (b) $Ca_xEu_{1-x}ZrO_3$, and (c) $Sr_xEu_{1-x}ZrO_3$ solid solutions.

Table 2 Néel Temperature (T_N), Curie temperature, (T_C), Weiss Temperature (θ_W), and saturation magnetization (M_S) of $A_xEu_{1-x}ZrO_3$

$Ba_xEu_{1-x}ZrO_3$	Transition temperature (K)	θ_W (K)	M_S (μ_B)
$x = 0.0$	$T_N = 4.1$	−0.19(2)	7.80(1)
$x = 0.1$	$T_N = 3.5$	0.11(1)	7.28(5)
$x = 0.2$		0.12 (1)	7.45(1)
$x = 0.3$	$T_C = 3.1$	0.67(1)	7.19(3)
$x = 0.4$		0.16(1)	7.33(3)
$x = 0.5$		0.15(2)	7.39(1)

$Ca_xEu_{1-x}ZrO_3$	Transition temperature (K)	θ_W (K)	M_S (μ_B)
$x = 0.0$	$T_N = 4.1$	−0.19(2)	7.80(1)
$x = 0.1$	$T_N = 4.0$	−0.22(1)	7.13(2)
$x = 0.2$	$T_N = 3.1$	−0.45(2)	7.07(2)
$x = 0.3$	$T_N = 3.0$	−0.86(1)	7.18(6)
$x = 0.4$	$T_N = 2.9$	−0.27(1)	7.31(4)
$x = 0.5$		−0.09(1)	7.58(2)

$Sr_xEu_{1-x}ZrO_3$	Transition temperature (K)	θ_W (K)	M_S (μ_B)
$x = 0.0$	$T_N = 4.1$	−0.19(2)	7.80(1)
$x = 0.1$	$T_N = 3.8$	−0.12(1)	7.31(10)
$x = 0.2$	$T_N = 3.3$	−0.07(1)	6.90(4)
$x = 0.3$	$T_N = 2.8$	−0.14(3)	6.98(1)
$x = 0.4$	$T_N = 2.2$	−0.09(1)	7.81(2)
$x = 0.5$		−0.075(7)	7.61(2)

Overall, the lattice expansion induced by the substitution of Ba^{2+} for Eu^{2+} inhibits the AFM interaction, leading to a situation that FM state is dominant. In contrast, enhancement of AFM interaction is realized through the lattice compression in $Ca_xEu_{1-x}ZrO_3$. For $Sr_xEu_{1-x}ZrO_3$, the value of θ_W is negative and increases to approach zero with an increase in the fraction of Sr. This phenomenon simply indicates that the magnetic structure is changed from AFM to PM by the dilution of magnetic moments belonging to Eu^{2+} because the lattic volume is almost independent of the composition of $Sr_xEu_{1-x}ZrO_3$ due to the fact that the ionic radius of Sr^{2+} and Eu^{2+} is almost the same as each other.

The magnetic field ($\mu_0 H$) dependence of magnetization (M) at 2 K for $A_xEu_{1-x}ZrO_3$ is illustrated in Fig. 5. The data at low $\mu_0 H$ are magnified in the insets. For $Sr_xEu_{1-x}ZrO_3$ at low $\mu_0 H$, the continuous increase of slope of the M–H curves indicates the gradual weakening of AFM interaction due to the dilution of Eu^{2+} ions. On the other hand, a decrease in the slope at low $\mu_0 H$ indicates an enhanced AFM interaction for $Ca_{0.3}Eu_{0.7}ZrO_3$. For $Ba_{0.3}Eu_{0.7}ZrO_3$, an abrupt increase in the slope at around 1000 Oe is found and the hysteresis loop is observed unlike $A_{0.3}Eu_{0.7}ZrO_3$ (A = Sr and Ca) in Fig. S5 (ESI†), corresponding to the FM states of $Ba_{0.3}Eu_{0.7}ZrO_3$ for Eu^{2+} spins. This FM state can also be confirmed by the steep increase of magnetic susceptibility with decreasing temperature below T_C when a magnetic field of 100 Oe is applied. Furthermore, Fig. 5 demonstrates that the saturation magnetization (M_S) for the $A_xEu_{1-x}ZrO_3$ series ranges from 7.19 μ_B to 7.80 μ_B (also summarized in Table 2). These values are almost identical to the theoretical magnetic moment of Eu^{2+} (7 μ_B), suggesting that almost all the europium ions are present as a divalent state in the $A_xEu_{1-x}ZrO_3$ solid solutions. This fact indicates that the reduction process of Eu^{3+} into Eu^{2+} by using ZrN is effective.

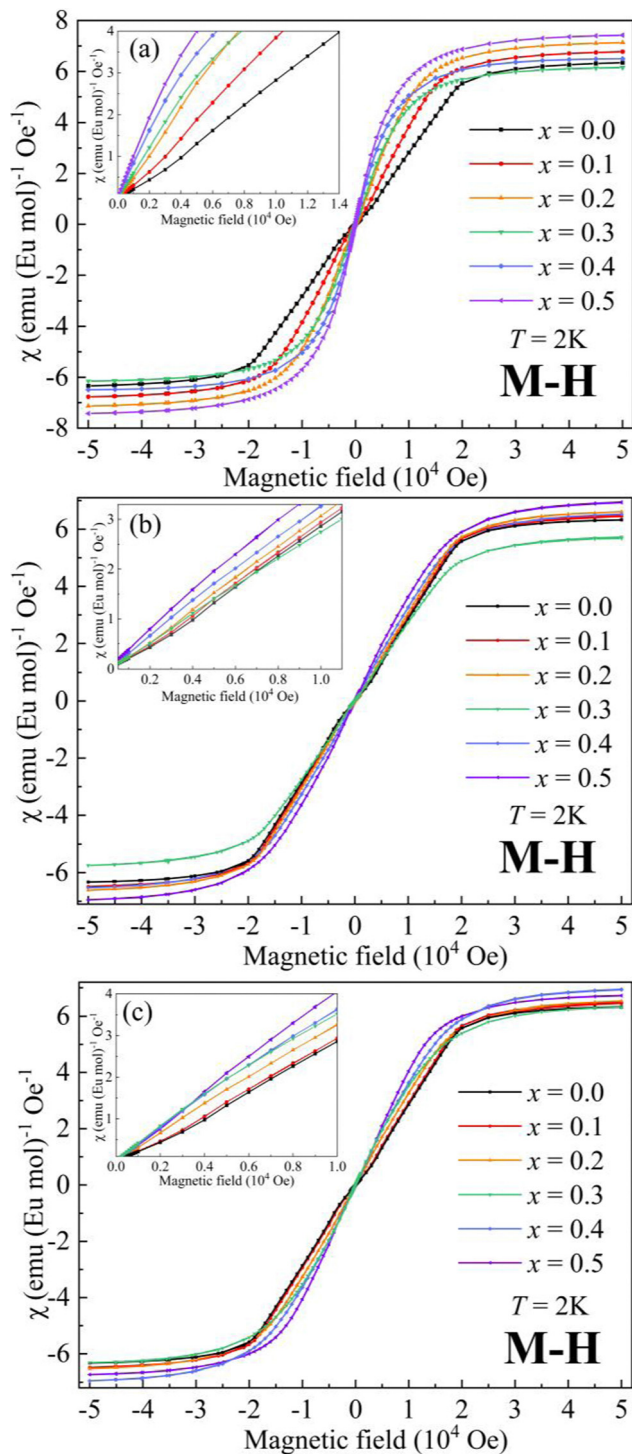by the magnetic dilution with an increase in the fraction of Sr, θ_W is gradually increased to approach 0 from a negative value with the increase of x. For $Ca_xEu_{1-x}ZrO_3$, θ_W is negative independent of the composition, suggesting that the AFM interaction is dominant in all the solid solutions of this system. There seems a tendency that θ_W deceases, takes a minimum at $x = 0.3$, and then increases as the fraction of Ca is increased.

8388 | *J. Mater. Chem. C*, 2023, **11**, 8383–8392

This journal is © The Royal Society of Chemistry 2023

Fig. 5 Dependence of magnetization on magnetic field at 2 K for (a) $Ba_xEu_{1-x}ZrO_3$, (b) $Ca_xEu_{1-x}ZrO_3$, and (c) $Sr_xEu_{1-x}ZrO_3$.

Fig. 6 The value of $\theta_W/(1-x)$, in which θ_W is Weiss temperature and x is the concentration ratio of alkaline earth metal elements, is plotted against the lattice volume. The dashed line represents the fitted linear regression line.

Since the linear relationship between the lattice volume and composition x is found, the compositional change can directly reflect the variation of lattice volume and accompanying crystal structural change of $EuZrO_3$. Therefore, the compositional dependence of magnetic properties and crystal structure can lead to the relationship between the lattice volume and
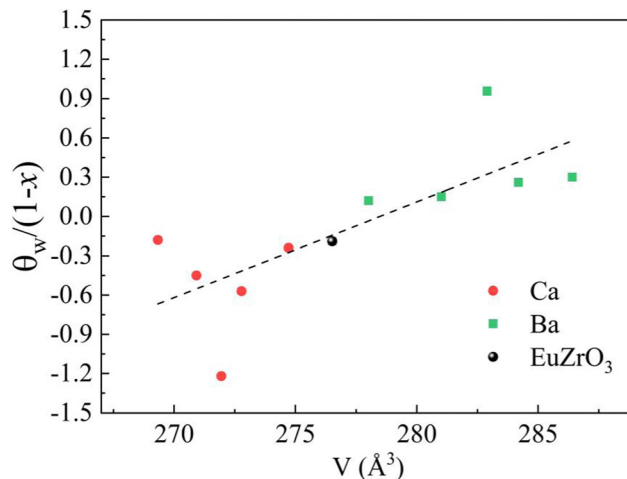
magnetic order. Here it should be noted that we can reasonably discuss magnetic properties at very low temperatures in terms of the crystal structure at room temperature because the crystal structure remains stable for $EuZrO_3$, $BaZrO_3$, $SrZrO_3$, and $CaZrO_3$ even when the temperature is varied from room temperature to very low temperature as described in section 2.1. According to the simple mean field theory, the Weiss temperature depends on the number of magnetic moment as well as the magnitude of magnetic interaction. Thus, it is thought that the parameter, $\theta_W/(1-x)$, reflects the magnitude of magnetic interaction between Eu^{2+} ions in the first approximation. In Fig. 6, we present the lattice volume dependence of $\theta_W/(1-x)$. It is found that $\theta_W/(1-x)$ is apt to increase with an increase in the lattice volume. It is worth noting that the tuning of magnetic interaction and the resultant magnetic transition are considered to be induced by the lattice expansion and shrinkage rather than the changes in crystal symmetry since the crystal structure retains orthorhombic $Pbnm$ in the range of lattice volume shown in Fig. 6. The results elucidate the relationship between the lattic volume and magnetic order which has been predicted by the theoretical calculations for $EuZrO_3$.[28]

2.3 Microscopic origin of magnetic behavior

To get a better understanding of the effect of the variation of lattice volume on the magnetic behavior, the origin and magnitude of the effect are discussed from a microscopic point of view. The cooperative rotation of ZrO_6 octahedra needs to be taken into account since it has been microscopically verified on the basis of first principles calculations that the octahedral rotation, related to the change of lattice volume of the orthorhombic structure, facilitates the AFM superexchange interactions between Eu^{2+} ions via vacant 4d state of Zr^{4+} in the orthorhombic $EuZrO_3$.[28] For the series of Ba-substituted solid solutions, an increase in the lattice volume is accompanied by the continuous conversion of the crystal structure from $Pbnm$
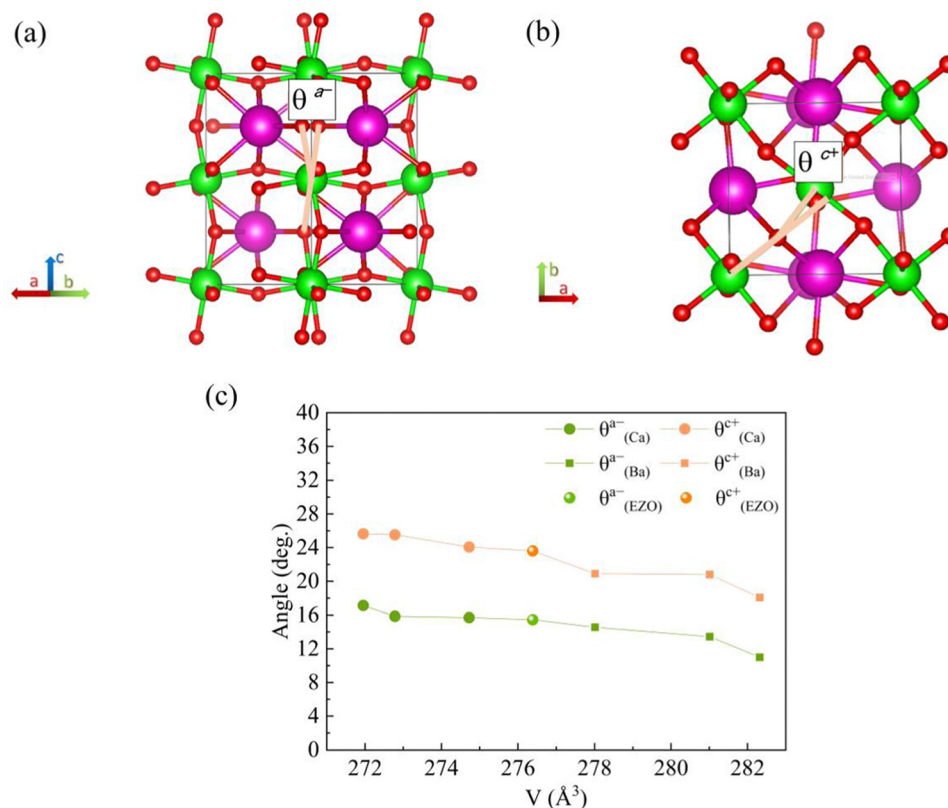
This journal is © The Royal Society of Chemistry 2023

J. Mater. Chem. C, 2023, 11, 8383–8392 | 8389

Fig. 7 Schematics of ZrO_6 octahedral rotations (tilt angles) along the (a) a-axis and (b) c-axis in an orthorhombic *Pbnm* structure ($a^-a^-c^+$). The europium atoms are shown as green spheres, the zirconium atoms as purple spheres and the oxygen atoms as red spheres. The rotation angles θ^{a-} and θ^{c+} are defined in (a) and (b), respectively. (c) The relation between the lattice volume and the octahedral rotation angles θ^{a-} and θ^{c+} for orthorhombic $Ca_xEu_{1-x}ZrO_3$ ($0 \leqq x \leqq 0.3$), $EuZrO_3$, $Ba_xEu_{1-x}ZrO_3$ ($0 \leqq x \leqq 0.3$), respectively.

($a^-a^-c^+$) to *Ibmm* ($a^-a^-c^0$), *I4/mcm* ($a^0a^0c^-$), and then *Pm3̄m* ($a^0a^0a^0$) at room temperature. For the series of Ca- and Sr-substituted solid solutions, the crystal structure retain *Pbnm* ($a^-a^-c^+$) even when the fraction of Ca and Sr is altered. Fig. 7 illustrates the octahedral rotations with two types of angles θ^{a-} and θ^{c+} and the relationship between these rotation angles and the lattice volume. Here the lattice volume and the corresponding θ^{a-} and θ^{c+} were extracted from the data for $EuZrO_3$, $Ba_xEu_{1-x}ZrO_3$ and $Ca_xEu_{1-x}ZrO_3$ solid solutions with the structure of *Pbnm* ($a^-a^-c^+$). It is found that both θ^{a-} and θ^{c+} are increased with the decrease of lattce volume. As the relationship between the magnetism and the lattice volume is verified in Fig. 6, the result shown in Fig. 7 indicates that the AFM interaction is weakened by descending the octahedral rotations, leading to the situation that the FM interaction is more dominant. Consequently, the present experimental result supports the theoretical suggestions that the octahedral rotation has great influence on the overlap between the Eu^{2+} 4f orbital and the Zr^{4+} 4d orbital and hence, changes the magnitude of AFM interaction between Eu^{2+} ions *via* 4d state of Zr^{4+} in $EuZrO_3$.

3. Conclusions

We experimentally provide an insight into the relative strengths of the competing magnetic interactions between Eu^{2+} ions in

$EuZrO_3$, which is dependent on the lattice volume and crystal structure, as suggested by the first principles calculations. The variation of lattice volume was realized by synthesizing $EuZrO_3$-based solid solutions; Eu^{2+} was replaced by alkaline-earth metal ions with different radii, that is Ba, Sr, and Ca. The experimental results indicate that the magnetic ground state of $EuZrO_3$ can be switched from AFM to FM by increasing the lattice volume. This is consistent with the first-principles calculations reported previously. Furthermore, the results also demonstrate that there is a strong coupling between the magnetic structure and the rotation of ZrO_6 octahedra. Specifically, the AFM superexchange interaction between Eu^{2+} ions *via* Zr 4d state is enhanced by the rotations of the ZrO_6 octahedra. The expansion of lattice volume and concomitant reduction of ZrO_6 octahedral rotation lead to the situation that the FM indirect exchange interaction *via* Eu^{2+} 5d state overcomes the AFM interaction *via* Zr^{4+} 4d state.

4. Experimental details

4.1. Sample preparation

Polycrystalline $A_xEu_{1-x}ZrO_3$ (A = Ba, Ca; $x \leq 0.9$ and Sr; $x \leq 0.5$) were synthesized by the conventional solid-state reaction method. The stoichiometric mixture of reagent-grade Eu_2O_3, ZrO_2, ACO_3, and ZrN (both 99.9% pure, sourced from Kanto

Chemicals, Japan) with the molar ratio of $2-2x$, $3+x$, $4x$ and $1-x$ was pressed into a pellet. The ZrN was added as a reducing agent to convert Eu^{3+} into Eu^{2+}. The pellet was sintered in a carbon crucible at 1300 °C for 10 h under a reducing atmosphere of Ar (97 vol%)/H_2 (3 vol%). The resultant $EuZrO_3$ pellet was greenish-yellow, while the solid solutions of $Ba_xEu_{1-x}ZrO_3$, $Ca_xEu_{1-x}ZrO_3$, and $Sr_xEu_{1-x}ZrO_3$ were light greenish, light yellow, and light greenish-yellow, respectively.

4.2. Measurements of structural and magnetic properties

The crystal structure and purity of the sintered materials were characterized by XRD at room temperature using Cu Kα radiation (RINT2500, Rigaku). Structural parameters were determined by Rietveld refinement of the X-ray diffraction data using RIETAN-FP.[59–61] In order to estimate the structural distortions related to the ZrO_6 octahedral rotations, the two rotation angles θ^{a-} and θ^{c+} shown in Fig. 7 were determined by performing VESTA based on the Rietveld refinement results.[27,62] The chemical valence states of europium ions in $A_xEu_{1-x}ZrO_3$ were examined using HRXRF spectroscopy, Eu_2O_3 was used as a reference for trivalent Eu ions. Peak position corrections were performed using Mn $K\alpha_{12}$ standard spectra for each sample measurement. A Savitzky-Golay smoothing method was used (smoothing points = 7) to pretreat data before analysis.[63] The valence state of europium ions of $EuZrO_3$ was evaluated using the ^{151}Eu Mössbauer spectrum in a standard transmission geometry at room temperature, which employed γ-ray source of $^{151}Sm_2O_3$. The velocity calibration was done with the magnetic hyperfine spectrum of α-Fe foil using ^{57}Co γ-ray source. In addition, the Mössbauer spectrum of EuF_3 was utilized as a Doppler velocity standard.[64] To understand the influence of structural change on the magnetic properties of solid-state solutions $A_xEu_{1-x}ZrO_3$, temperature and magnetic field dependence of magnetization was measured using the superconducting quantum interference device magnetometer (MPMS, Quantum Design). The temperature dependence of magnetic susceptibilities was measured in a range of 2–300 K under both ZFC and FC processes at an external magnetic field of 100 Oe. The field dependence of magnetization was recorded at 2 K under magnetic fields up to 5 T.

Conflicts of interest

There are no conflicts to declare.

Acknowledgements

Notes and references

1 H. Schmid, *Ferroelectrics*, 1994, **162**, 317–338.
2 R. Ramesh and N. A. Spaldin, *Nat. Mater.*, 2007, **6**, 21–29.
3 N. A. Spaldin and R. Ramesh, *Nat. Mater.*, 2019, **18**, 203–212.
4 J. Wang, J. Neaton, H. Zheng, V. Nagarajan, S. Ogale, B. Liu, D. Viehland, V. Vaithyanathan, D. Schlom and U. Waghmare, *Science*, 2003, **299**, 1719–1722.
5 T. Kimura, T. Goto, H. Shintani, K. Ishizaka, T.-H. Arima and Y. Tokura, *Nature*, 2003, **426**, 55–58.
6 H. Akamatsu, K. Fujita, H. Hayashi, T. Kawamoto, Y. Kumagai, Y. Zong, K. Iwata, F. Oba, I. Tanaka and K. Tanaka, *Inorg. Chem.*, 2012, **51**, 4560–4567.
7 T. Katsufuji and H. Takagi, *Phys. Rev. B: Condens. Matter Mater. Phys.*, 2001, **64**, 054415.
8 A. Bussmann-Holder, E. Liarokapis and K. Roleder, *Sci. Rep.*, 2021, **11**, 1–8.
9 H. Wu and W. Shen, *Solid State Commun.*, 2005, **133**, 487–491.
10 P. Ryan, J. Kim, T. Birol, P. Thompson, J. Lee, X. Ke, P. Normile, E. Karapetrova, P. Schiffer and S. Brown, *Nat. Commun.*, 2013, **4**, 1–8.
11 T. Kolodiazhnyi, K. Fujita, L. Wang, Y. Zong, K. Tanaka, Y. Sakka and E. Takayama-Muromachi, *Appl. Phys. Lett.*, 2010, **96**, 252901.
12 H. Akamatsu, Y. Kumagai, F. Oba, K. Fujita, H. Murakami, K. Tanaka and I. Tanaka, *Phys. Rev. B: Condens. Matter Mater. Phys.*, 2011, **83**, 214421.
13 M. Itoh, T. Shimura, J.-D. Yu, T. Hayashi and Y. Inaguma, *Phys. Rev. B: Condens. Matter Mater. Phys.*, 1995, **52**, 12522.
14 T. Ishihara, H. Matsuda and Y. Takita, *J. Am. Chem. Soc.*, 1994, **116**, 3801–3803.
15 P. Radaelli, G. Iannone, M. Marezio, H. Hwang, S. Cheong, J. Jorgensen and D. Argyriou, *Phys. Rev. B: Condens. Matter Mater. Phys.*, 1997, **56**, 8265.
16 M. Uehara, S. Mori, C. Chen and S.-W. Cheong, *Nature*, 1999, **399**, 560–563.
17 J. Haeni, P. Irvin, W. Chang, R. Uecker, P. Reiche, Y. Li, S. Choudhury, W. Tian, M. Hawley and B. Craigo, *Nature*, 2004, **430**, 758–761.
18 K. J. Choi, M. Biegalski, Y. Li, A. Sharan, J. Schubert, R. Uecker, P. Reiche, Y. Chen, X. Pan and V. Gopalan, *Science*, 2004, **306**, 1005–1009.
19 M.-W. Chu, I. Szafraniak, R. Scholz, C. Harnagea, D. Hesse, M. Alexe and U. Gösele, *Nat. Mater.*, 2004, **3**, 87–90.
20 D. G. Schlom, L.-Q. Chen, C.-B. Eom, K. M. Rabe, S. K. Streiffer and J.-M. Triscone, *Annu. Rev. Mater. Res.*, 2007, **37**, 589–626.
21 D. G. Schlom, L.-Q. Chen, C. J. Fennie, V. Gopalan, D. A. Muller, X. Pan, R. Ramesh and R. Uecker, *MRS Bull.*, 2014, **39**, 118–130.
22 Y. Yokoyama, Y. Yamasaki, M. Taguchi, Y. Hirata, K. Takubo, J. Miyawaki, Y. Harada, D. Asakura, J. Fujioka and M. Nakamura, *Phys. Rev. Lett.*, 2018, **120**, 206402.
23 C. J. Fennie and K. M. Rabe, *Phys. Rev. Lett.*, 2006, **97**, 267602.

This journal is © The Royal Society of Chemistry 2023

J. Mater. Chem. C, 2023, **11**, 8383–8392 | 8391

24 J. H. Lee, L. Fang, E. Vlahos, X. Ke, Y. W. Jung, L. F. Kourkoutis, J.-W. Kim, P. J. Ryan, T. Heeg and M. Roeckerath, *Nature*, 2010, **466**, 954–958.

25 K. Kugimiya, K. Fujita, K. Tanaka and K. Hirao, *J. Magn. Magn. Mater.*, 2007, **310**, 2268–2270.

26 K. Fujita, N. Wakasugi, S. Murai, Y. Zong and K. Tanaka, *Appl. Phys. Lett.*, 2009, **94**, 062512.

27 Y. Lin, E.-M. Choi, P. Lu, X. Sun, R. Wu, C. Yun, B. Zhu, H. Wang, W. Li and T. Maity, *ACS Appl. Mater. Interfaces*, 2020, **12**, 8513–8521.

28 H. Akamatsu, Y. Kumagai, F. Oba, K. Fujita, K. Tanaka and I. Tanaka, *Adv. Funct. Mater.*, 2013, **23**, 1864–1872.

29 K. Tanaka, K. Fujita, Y. Maruyama, Y. Kususe, H. Murakami, H. Akamatsu, Y. Zong and S. Murai, *J. Mater. Res.*, 2013, **28**, 1031–1041.

30 R. Zhao, C. Yang, H. Wang, K. Jiang, H. Wu, S. Shen, L. Wang, Y. Sun, K. Jin and J. Gao, *Nat. Commun.*, 2022, **13**, 2364.

31 M. Shafer, *J. Appl. Phys.*, 1965, **36**, 1145–1152.

32 A. M. Glazer, *Acta Crystallogr., Sect. B: Struct. Crystallogr. Cryst. Chem.*, 1972, **28**, 3384–3392.

33 V. Viallet, J.-F. Marucco, J. Saint, M. Herbst-Ghysel and N. Dragoe, *J. Alloys Compd.*, 2008, **461**, 346–350.

34 Y. Zong, K. Fujita, H. Akamatsu, S. Murai and K. Tanaka, *J. Solid State Chem.*, 2010, **183**, 168–172.

35 B. Alho, E. Nóbrega, V. de Sousa, A. M. G. Carvalho, N. De Oliveira and P. Von Ranke, *J. Appl. Phys.*, 2011, **109**, 083942.

36 J. Coey, M. Viret and S. Von Molnar, *Adv. Phys.*, 1999, **48**, 167–293.

37 G. Cuono, F. Forte, A. Romano, X. Ming, J. Luo, C. Autieri and C. Noce, *Phys. Rev. Mater.*, 2021, **5**, 064402.

38 B. Kennedy, C. Howard, G. Thorogood and J. Hester, *J. Solid State Chem.*, 2001, **161**, 106–112.

39 L. Li, B. J. Kennedy, Y. Kubota, K. Kato and R. F. Garrett, *J. Mater. Chem.*, 2004, **14**, 263–273.

40 C. J. Howard, G. R. Lumpkin, R. I. Smith and Z. Zhang, *J. Solid State Chem.*, 2004, **177**, 2726–2732.

41 N. L. Henderson, X. Ke, P. Schiffer and R. E. Schaak, *J. Solid State Chem.*, 2010, **183**, 631–635.

42 Y. Ren, R. Küngas, R. J. Gorte and C. Deng, *Solid State Ion.*, 2012, **212**, 47–54.

43 M. Y. Liu, T. L. Sun, X. L. Zhu, X. Q. Liu, H. Tian and X. M. Chen, *J. Am. Ceram. Soc.*, 2021, **104**, 6393–6403.

44 H. D. Megaw, *Proc. Phys. Soc.*, 1946, **58**, 133.

45 H. Koopmans, G. Van De Velde and P. Gellings, *Acta Crystallogr., Sect. C: Cryst. Struct. Commun.*, 1983, **39**, 1323–1325.

46 B. J. Kennedy, C. J. Howard and B. C. Chakoumakos, *Phys. Rev. B: Condens. Matter Mater. Phys.*, 1999, **59**, 4023.

47 A.-M. Azad, S. Subramaniam and T. W. Dung, *J. Alloys Compd.*, 2002, **334**, 118–130.

48 R. D. Shannon, *Acta Crystallogr., Sect. A: Cryst. Phys., Diffr., Theor. Gen. Crystallogr.*, 1976, **32**, 751–767.

49 M. Avdeev, B. J. Kennedy and T. Kolodiazhnyi, *J. Condens. Matter Phys.*, 2014, **26**, 095401.

50 K. Knight, *J. Mater. Sci.*, 2020, **55**, 6417–6428.

51 A. Shukla, V. Parey and N. Gaur, *AIP Conf. Proc.*, 2016, 020011.

52 E. Slonimskaya and A. Belyakov, *Glass Ceram.*, 2001, **58**, 54–56.

53 C. J. Howard and H. T. Stokes, *Acta Crystallogr., Sect. B: Struct. Sci.*, 1998, **54**, 782–789.

54 L. Vegard, *Z. Phys.*, 1921, **5**, 17–26.

55 A. R. Denton and N. W. Ashcroft, *Phys. Rev. A: At., Mol., Opt. Phys.*, 1991, **43**, 3161.

56 J. Van Vleck, *The Theory of Electric and Magnetic Susceptibilities*, Clarendon, Oxford, 1932.

57 L. Holmes, R. Sherwood, L. Van Uitert and S. Hüfner, *Phys. Rev.*, 1969, **178**, 576.

58 Y. Zong, K. Fujita, H. Akamatsu, S. Murai and K. Tanaka, *Phys. Status Solidi C*, 2011, **8**, 3051–3054.

59 H. Rietveld, *Acta Crystallogr.*, 1967, **22**, 151–152.

60 D. L. Bish and S. Howard, *J. Appl. Crystallogr.*, 1988, **21**, 86–91.

61 F. Izumi and K. Momma, *Solid State Phenom.*, 2007, 15–20.

62 K. Momma and F. Izumi, *J. Appl. Crystallogr.*, 2011, **44**, 1272–1276.

63 T. Konishi, J. Kawai, M. Fujiwara, T. Kurisaki, H. Wakita and Y. Gohshi, *X-Ray Spectrom.*, 1999, **28**, 470–477.

64 G. Shenoy and B. Dunlap, *Nucl. Instrum. Methods*, 1969, **71**, 285–291.

8392 | *J. Mater. Chem. C*, 2023, **11**, 8383–8392

This journal is © The Royal Society of Chemistry 2023